Lipid zonation and phospholipid remodeling in non-alcoholic fatty liver disease

Zoe Hall[1,2], Nicholas J. Bond[2], Tom Ashmore[1], Francis Sanders[2], Zsuzsanna Ament[2], Xinzhu Wang[1], Andrew J. Murray[3], Elena Bellafante[4], Sam Virtue[5], Antonio Vidal-Puig[5], Michael Allison[6], Susan E. Davies[7], Albert Koulman[2], Michele Vacca[1, 2, 5], Julian L. Griffin[1,2,*]

[1] Department of Biochemistry and Cambridge Systems Biology Centre, University of Cambridge, 80 Tennis Court Road, Cambridge, CB2 1GA, UK

[2] MRC Human Nutrition Research, 120 Fulbourn Road, Cambridge, CB1 9NL, UK

[3] Department of Physiology, Development and Neuroscience, University of Cambridge, Downing Street, Cambridge, CB2 3EG, UK

[4] Fondazione Mario Negri Sud, Santa Maria Imbaro, Chieti, Italy

[5]Metabolic Research Laboratories, Wellcome Trust-MRC Institute of Metabolic Science, Addenbrooke's Hospital, University of Cambridge, Cambridge, CB2 0QQ, UK

[6] Liver Unit, Department of Medicine, Cambridge University Hospitals NHS Foundation Trust, Cambridge, CB2 0QQ, UK

[7] Department of Histopathology, Cambridge University Hospitals NHS Foundation Trust, Cambridge, CB2 0QQ, UK

Keywords: mass spectrometry imaging; lipidomics; eicosanoids; arachidonic acid; NASH

Corresponding Author Contact Information:

Julian L. Griffin; Department of Biochemistry and Cambridge Systems Biology Centre, University of Cambridge, 80 Tennis Court Road, Cambridge, CB2 1GA, United Kingdom; Tel: +44 (0) 1223 764922;

jlg40@ cam.ac.uk

List of Abbreviations:

NAFLD – non-alcoholic fatty liver disease; NAFL – non-alcoholic fatty liver; NASH – non-alcoholic steatohepatitis; AA – arachidonic acid; LOX – lipoxygenase; LPCAT – lysophoshatidylcholine acyl transferase ; TAG – triacylglyceride; DAG – diacylglyceride; MUFA – monounsaturated fatty acid; PC – phosphatidylcholine; PUFA – polyunsaturated fatty acid; SFA – saturated fatty acid; MSI – mass spectrometry imaging; MALDI – matrix assisted laser desorption ionisation; cPLA2 – group IVA phospholipase A2; HETE - hydroxyeicosatetranoic acid; Alox15 – arachidonate 15-lipoxygenase; WT – wild type; HF – high fat; RC – regular chow; WD – Western diet; LFD – low fat diet; MCD - methionine choline deficient; MCS – methionine choline sufficient; CID – collision induced dissociation; SEM – standard error of mean; Rn18s – 18s ribosomal RNA; Alox5 - arachidonate 5-lipoxygenase; Alox12 - arachidonate 12-lipoxygenase; ACTB – beta actin; PCA – principal components analysis; OPLS-DA - orthogonal projection to latent structures discriminant analysis; PE – phosphatidylethanolamine; PI – phosphatidylinositol; PG – phosphatidylglycerol; PS – phosphatidylserine; SM – sphingomyelin; FFA - free fatty acid; LA – linoleic acid; DHA - docosahexaenoic acid; HODE - hydroxyoctadecadienoic acid; EPA - eicosapentaenoic acid ; HEPE - hydroxyeicosapentaenoic acid; HDoHE - hydroxydocosahexaenoic acid.

Financial Support: JLG, ZH, NJB, AK, MV & ZA are funded by the Medical Research Council (Lipid Profiling and Signalling, MC UP A90 1006 & Lipid Dynamics and Regulation, MC PC 13030). AVP, MA and MV are members of the EPoS (Elucidating Pathways of Steatohepatitis) consortium funded by the Horizon 2020 Framework Program of the European Union under Grant Agreement 634413. AVP, SV and MV are also supported by MRC MDU and MRC DMC (MC UU 12012/2). MA, AVP and JLG gratefully acknowledge the Evelyn Trust and the Cambridge Biomedical Research Centre for research support.

Abstract

Non-alcoholic fatty liver disease (NAFLD) can progress from 'simple steatosis' (NAFL) to non-alcoholic steatohepatitis (NASH), cirrhosis and cancer. Currently the driver for this progression is not fully understood; in particular it is not known how NAFLD and its early progression affects the distribution of lipids in the liver, producing lipotoxicity and inflammation. Here we use dietary and genetic mouse models of NAFL and NASH, and translate results to humans, by correlating the spatial distribution of lipids in liver tissue with disease progression, using advanced mass spectrometry imaging technology. We identified several lipids with distinct zonal distributions in control and NAFL samples, whilst partial to complete loss of lipid zonation was found in NASH. In addition, we found increased hepatic expression of genes associated with remodelling the phospholipid membrane, release of arachidonic acid (AA) from the membrane, and production of eicosanoid species which promote inflammation and cell injury. Using immunohistochemistry, we further suggest that the zonal location of remodelling enzyme lysophosphatidylcholine acyl transferase 2 (LPCAT2) plays a role in the change in spatial distribution for arachidonic acid (AA)-containing lipids. This results in a cycle of AA-enrichment in pericentral hepatocytes, membrane release of AA and generation of pro-inflammatory eicosanoids, and may account for increased oxidative damage in pericentral regions in NASH. ***Conclusion:*** We have demonstrated that NAFLD is associated not only with lipid enrichment, but also to zonal changes of specific lipids and their associated metabolic pathways. This may play a role in the heterogeneous development of NAFLD.

Introduction

Non-alcoholic fatty liver disease (NAFLD) is characterised by accumulation of triacylglycerides (TAG) in the liver (steatosis); however a subgroup of patients will progress to more serious conditions, including non-alcoholic steatohepatitis (NASH), cirrhosis, hepatocarcinoma and liver failure (1-4). A 'multiple-hit' process for NAFLD has been suggested, whereby fatty liver is followed by oxidative stress and lipid peroxidation leading to an inflammation cascade, cell injury and the development of NASH (5). However, the detailed mechanisms underlying disease progression remain poorly understood.

Given that NAFLD is characterised by an imbalance in lipid homeostasis, lipidomics approaches are well placed to interrogate the specific changes associated with this disease (6). Previous studies have concentrated on discovering biomarkers to differentiate between 'healthy' fatty liver (NAFL) and NASH (7-9), and to establish changes to the lipidome with progression of NAFLD (10, 11). However, many of these previous studies have focussed on circulating markers for liver disease, and hence are distal to the actual pathophysiology, or rely on tissue extracts that ignore the heterogeneous nature of the disease.

Different zones exist in the liver lobules according to proximity to the portal triad - the main supplier of nutrient and oxygen-rich blood to the liver. In addition to a gradient of nutrients and oxygen, zonation of glucose and fatty acid metabolism has been observed (12). Whilst hepatocytes closest to the portal vein (periportal or zone 1) are more involved in gluconeogenesis and β-oxidation of fatty acids, glycolysis and lipogenesis occur at a higher rate in hepatocytes closest to the central vein (pericentral or zone 3) (12). Furthermore, steatosis in adult NAFL and oxidative damage to cells in NASH are chiefly localised to pericentral regions (1). As a consequence, lipids are distributed differentially within the liver lobule; however, little is known on how the development and progression of NAFLD affects lipid zonation and metabolism. Proof-of-principle studies have shown that mass

spectrometry imaging (MSI), a transformative technology enabling the *in situ* analysis of tissue molecular composition (13-15), can detect the differential distribution of lipids in both healthy and steatotic liver tissue (16-18).

Here we study dietary and genetic models of NAFL and NASH in mice to complement a set of human liver biopsies. Using matrix assisted laser desorption ionisation (MALDI) MSI, coupled with lipidomics techniques and bioinformatics tools, we monitored subtle changes in the distribution and abundance of lipids as a function of their location within the liver lobule. We found several lipids with distinct distributions in control and NAFL liver, along with an increase in pro-inflammatory arachidonic acid (AA)-derived lipoxygenase (LOX) metabolites. Progression to NASH however, led to increasing loss of lipid zonation.

We further found increased hepatic mRNA levels in both mouse and human NAFLD samples for genes associated with membrane remodelling (*LPCAT2, cPLA2*) and eicosanoid production (*ALOX15*). Additionally, immunostaining revealed that lysophosphatidylcholine acyl transferase 2 protein (LPCAT2), which is responsible for incorporation of AA into the membrane, had a distinct pericentral distribution in human liver. Upregulation of LPCAT2 in NAFLD may therefore be a potential driving force behind enrichment of AA in pericentral hepatocytes, enabling the phospholipid membrane to serve as a substrate pool for free AA and its eicosanoid metabolites. This study is the first to suggest the potential importance of the physical location of intact lipids and their associated metabolic pathways in the pathology of NAFLD.

Experimental Procedures

Mouse samples

High fat diet: Five-week old male *ob/ob* (N=5) and wild type (WT, C57BL/6J strain, N=5) mice were maintained on a high fat diet or regular chow diet for 12 weeks. High fat diet caloric content was 55% fat, 29% protein, 16% carbohydrate (diet code: 829197; Special Diet Services, UK). Regular chow diet caloric content was 11.5% fat, 26.9% protein, 61.6% carbohydrate (RM1; Special Diet Services, UK).

Western diet: Eight-week old male WT (C57BL/6J strain) mice were maintained on a western diet (N=5/time point; adjusted calories diet code: TD.88137; caloric content: 42.0 % fat, 15.2 % protein, 42.7 % carbohydrate, 0.2 % cholesterol; Harlan Laboratories, Madison) or low fat control diet (N=5/time point; TD 08485; caloric content: 13 % fat, 19.2% protein, 67.9 % carbohydrate; Harlan Laboratories, Madison) for 12 or 32 weeks.

Methionine choline deficient diet: Eight-week old male WT mice (FVB/N strain) were fed MCD high-fat diet (N=5; D12451, Research Diets) or MCS control diet (N=5) for 8 weeks as described previously (19).

Mice were euthanized, and the liver tissue rapidly dissected and snap-frozen. Liver enzyme activity assays were performed on collected serum. All animal protocols were approved by the UK Home Office and the University of Cambridge Animal Welfare and Ethical Review Board, and carried out by a personal licence holder.

Human samples

Twenty-three human samples were obtained from the Human Research Tissue Bank, at Addenbrooke's Hospital, Cambridge (Cambridgeshire 2 Research Ethics Committee, NRES 11/EE/0011). Samples were scored contemporaneously by an experienced histopathologist for steatosis (0-3), ballooning (0-2), inflammation (0-2), fibrosis (0-4) and were diagnosed according to the SAF system (20). Samples were thus classified as normal (N=2), NAFL (N=11), borderline minimal NASH

(N=4), moderate NASH (N=5) and cirrhosis (N=1). All samples were analysed, but for the purposes of statistics, comparisons were made between two groups: NAFL (N=11) and borderline NASH/NASH (N=9), hereafter referred to as NASH.

MALDI Imaging MS

Mouse and human liver samples were embedded in Tissue-Tek® OCT™ and 10 μm frozen sections on glass microscope slides were prepared using a cryostat. Adjacent sections were stained with haematoxylin and eosin (H&E) or Masson's trichrome. Tissue sections were washed with 50 mM potassium nitrate (5 s) prior to matrix application in order to form exclusively potassiated adducts (**Figure S1A**) to reduce spectral complexity (a combination of K^+, Na^+ and H^+ adducts are normally detected with MALDI). Matrix solutions (10 mg/mL) of 2, 5-dihydroxybenzoic acid (DHB; Sigma-Aldrich, St Louis, MO) were prepared in 85:15 methanol: water (*v/v*) and administered to the tissue surface using a nebulised sprayer (Suncollect MALDI spotter, KR Analytical Ltd, Cheshire, UK). Imaging experiments were carried out for three biological replicates per group (mouse) and all human samples using a MALDI LTQ Orbitrap XL (Thermo Fisher Scientific) at 50 μm step increments across the tissue. Spectra were acquired in positive ion mode, from 250-1000 *m/z* at 60,000 resolution. Lipid identity was performed by accurate mass using the LipidMaps database (21). The predominant fatty acid composition was confirmed where possible by tandem MS using collision-induced dissociation (CID). In order to improve fragmentation, lithium adducts with more efficient fragmentation (22) were formed by a 5 s washing step in lithium nitrate (50 mM) prior to deposition of matrix, and the corresponding lithiated ions subjected to fragmentation (**Figure S1B**).

Lipidomics

Lipids were extracted using an adaptation of the Folch method (23). Briefly, 400 μL of deionised water was added to 30 mg of liver tissue and homogenised using a TissueLyser (Qiagen Ltd., Manchester, UK). Chloroform: methanol (2:1, 1 mL) was added and the samples vortexed and centrifuged (12,000 *g*, 10 min). The extraction was performed twice, and the resulting organic layers were combined, dried under nitrogen and reconstituted in chloroform: methanol (2:1, 300 μL). Prior to analysis, samples (20 μL) were diluted in isopropanol: acetonitrile: water (2: 1: 1, 980 μL).

Samples were analysed by liquid chromatography-mass spectrometry (LC-MS) using an Accela Autosampler (Thermo Scientific, Hemel Hempstead, UK) coupled to a LTQ Orbitrap Elite™ (Thermo Scientific). Five μL of sample was injected onto an Acuity C18 BEH column (Waters Ltd., Warrington, UK; 50 × 2.1 mm, 1.7 μm) maintained at 55 °C. Mobile phase A was 100 mM ammonium formate in acetonitrile: water 60:40 and mobile phase B was 100 mM ammonium formate in isopropanol: acetonitrile 90:10 . The flow rate was 0.5 mL/min; the mobile phase gradient is detailed in **Table S1**. A heated electrospray ionisation source was maintained at 375 ˚C, the desolvation temperature was 380 ˚C and desolvation gas flow at 40 arbitrary units. Spectra were acquired in positive and negative ion mode in the range of 100 - 2000 *m/z*.

Gas chromatography-mass spectrometry

Liver tissue or pellets of feed were extracted as described above. Total fatty acids in the dried lipid extract (200 μL) were derivatized using methanolic boron trifluoride (14 %, 125 μL). Chloroform: methanol (1:1, 100 μL) was added, and the samples heated to 80 **°**C for 90 mins. After cooling, deionised water (300 μL) and hexane (600 μL) were added to each sample. The upper organic fractions were separated, dried under nitrogen and reconstituted in hexane (200 μL) for analysis.

A 7683 series autosampler (Agilent Technologies, Santa Clara, CA, USA) coupled to a 7683B Injector (Agilent Technologies, Santa Clara, CA, USA) was used to inject 1 μL of sample onto an HP88 GC column (Agilent Technologies) (88% - cyanopropyl aryl-polysiloxane, 0.17 μm thickness, 320 μm diameter, 50 m length). The injector temperature was 250 °C using a split ratio of 10:1, and flow rate of helium was 12 mL/min. An initial temperature of 100 °C was held for 1 min, followed by a temperature ramp of 10 °C/min to 300 °C, maintained for 2 min. Data were acquired after a solvent delay of 4 min (60 - 400 *m/z*).

Eicosanoid assay

Eicosanoids were extracted from homogenised tissue (50 mg) as described previously (24). Samples were analysed by LC-MS/MS on a 5500 QTRAP (ABSciex UK Limited, Warrington, UK) coupled to an ACQUITY system (Waters Ltd., Warrington, UK). Samples were injected (10 μL) onto a Kinetex 2.6 μm XB-C18 100 Å column (100 x 2.1 mm, Phenomenex, Macclesfield, UK) at 30 °C. Mobile phase A consisted of 0.1 % acetic acid in water, whilst mobile phase B was 0.1 % acetic acid in 80:20 acetonitrile: methanol (0.5 mL/min, gradient in **Table S2**). The electrospray source was operated in negative ion mode (4.5 kV and 650 °C). Mass transitions of 51 analytes and 3 isotopically labelled standards (**Table S3**) were acquired. Peaks were integrated within Analyst™ version 1.6 and normalised against wet tissue weight and isotopically labelled internal standard; quantification was performed using available standards (Cayman Chemical Company).

Transcript quantification

Total RNA was purified from frozen human and mouse liver using a RNeasy Mini Kit (Qiagen). Briefly, approximately 20 mg tissue samples were lysed and homogenised in Trizol (1 mL) using a TissueLyzer

(Qiagen). The samples were centrifuged at 12,000 *g* for 15 min following the addition of chloroform (200 µL) and the RNA-containing aqueous phase combined with 1 volume of 70 % ethanol. Samples were loaded on spin columns and procedure continued as per the manufacturer guidelines. Purified RNA concentration was quantified (260 nm) using a NanoDrop 100 (Thermo Fisher Scientific). Genomic DNA contamination was eliminated using RT^2 First Strand Kit (Qiagen) and complimentary DNA produced using RT^2 First Strand Kit (Qiagen). Relative abundance of transcripts of interest was assessed by quantitative-PCR in RT^2 SYBRgreen Mastermix (Qiagen) with a StepOnePlus detection system (Applied Biosciences, Warrington, UK). RT^2 primer assays for mouse *Rn18s* (endogenous control), c*Pla2*, *Lpcat2*, *Alox5*, *Alox12, Alox15, Tnf-*α*, Tgb-*β*1* and human *ACTB* (endogenous control), c*PLA2, LPCAT2 and ALOX15* were obtained from Qiagen. Thermocycler (PTC-200, MJ Research) parameters were: incubation, 95 °C for 10 min; elongation, 95 °C for 15 s; and cooling, 60 °C for 1 min. Elongation and cooling underwent 40 cycles. Expression levels were normalised to endogenous controls using the $\Delta\Delta C_T$ method.

Immunohistochemistry

Immunostaining was performed on 10 µm frozen sections, fixed in cold acetone using the Rabbit VECTASTAIN ELITE ABC horseradish peroxidase kit (Vector Laboratories Ltd, Peterborough, UK) following the manufacturer's protocol. Counter-staining was performed using haematoxylin (Sigma-Aldrich). Primary antibodies were anti-LPCAT2 (Atlas Antibodies, Stockholm, Sweden; HPA007891; 1:200 (mouse) 1:500 (human)) and anti-CD68 (Abcam, Cambridge, UK; ab955; 1:250).

Data processing

Lipidomics: Data were converted to mzML format for subsequent data processing, and features were picked using an in-house R script. Principal components analysis (PCA) and orthogonal projection to

latent structures discriminant analysis (OPLS-DA) models (25, 26) were constructed using SIMCA 14 (Umetrics, Sweden), following normalisation to the total ion count, and Pareto scaling (27).

MALDI-MSI: Each MALDI-MSI experiment is composed of multidimensional data, whereby every pixel (*x*, *y* coordinate) is associated with a mass spectrum (*m/z*, intensities). Data from MALDI-MSI were converted to imzML format for processing (28). Using an in-house R script, ions were retained above a threshold intensity and the *m/z* ratio of ions detected were summed across integral regions of 10 ppm to allow for alterations in *m/z* mass accuracy across the experiment ("binning"). Ion intensities were normalised to total ion count, mean centred and Pareto scaled before production of single ion images or multivariate statistical analysis (PCA). During PCA, pixels can be considered analogous to "observations" and *m/z* values to "variables". PC loadings were normalised according to their contribution to the overall variation prior to computing averages from different experiments. Multi-ion image overlays were produced using ImageQuest software (Thermo Fisher Scientific).

Univariate statistics: Unless stated otherwise, data is reported as mean value ± standard error of mean (SEM). Statistical significance was evaluated using ANOVA with Tukey's *post-hoc* test.

Results

Hepatic lipid signatures change with NAFL

We induced NAFL in mice using dietary and genetic models: WT and *ob/ob* mice were maintained on a high fat (HF) or regular chow (RC) diet. WT (C57BL/6J strain) mice are susceptible to diet-induced obesity and develop NAFL when fed a HF diet (29), whilst *ob/ob* mice lack the ability to produce leptin, presenting a phenotype of obesity and insulin resistance, and spontaneously develop steatosis (29, 30). Body weights for the four groups were measured after 12 weeks and found to increase in the order: WT-RC < WT-HF << *ob/ob*-RC < *ob/ob*-HF (31). NAFL was induced in the WT-HF and *ob/ob* mice, and was characterised by zone 3 macrovesicular steatosis, with the amount of steatosis greatest in the *ob/ob*-RC and *ob/ob*-HF groups (**Figure 1A**). Early signs of inflammation and cell injury were observed (**Figure 1B**), including increased liver enzymes and expression of pro-inflammatory cytokine *Tnf-*α and pro-fibrotic factor *Tgf-*β*1*.

In order to determine whether the lipid signatures in liver tissue would enable the distinction of the groups above, we performed lipidomics experiments. Lipids were extracted from homogenised tissue and analysed by LC-MS. Overall in positive and negative ion modes, over 800 lipids were identified from 11 classes, including TAGs, diacylglycerides (DAG), phosphatidylcholines (PC), phosphatidylethanolamines (PE), phosphatidylinositols (PI), phosphatidylglycerols (PG), phosphatidylserines (PS), sphingomyelins (SM), cholesteryl esters and free fatty acids (FFA). As expected, the most striking observation was the relative increase in TAGs compared to PCs in NAFL liver compared to control (**Figure 1C-1D**). Identified lipids were used to construct a PCA model, which successfully discriminated the four sample groups (R^2 = 0.93, Q^2 = 0.90; **Figure 1E**). The first principal component related primarily to the disease status (NAFL or normal), whilst the second principal component differentiated the diets. The corresponding loadings plot (**Figure 1F**) revealed the lipid species most influential in distinguishing groups. These included a relative increase in PCs and

saturated fatty acids (SFA) for WT-RC control liver tissue; and a relative increase in TAGs and monounsaturated fatty acids (MUFA), particularly FFA(18:1), for the NAFL groups. The high fat diet groups had a greater proportion of polyunsaturated fatty acids (PUFA) and TAGs with longer chain length and greater unsaturation. In contrast, the *ob/ob*-RC group had the highest FFA(18:1) content of all four groups, and shorter chain TAGs.

Next we carried out GC-MS to determine the total fatty acid profiles of liver tissue from the different groups, and to compare these with the profiles from the HF and RC feed (**Figure S2, Table S4**). Interestingly, the MUFA: SFA ratio was similar in the HF and RC diets, whilst increasing up to 4-fold in *ob/ob*-RC mice compared to WT-RC controls. This suggests that the increased hepatic MUFA is due to an increase in production through *de novo* lipogenesis (DNL) (4) and stearoyl co-A desaturase 1 (SCD1) activity. We calculated a proxy for increased SCD1 activity (32), and found this to be increased in *ob/ob* compared to WT mice, with the greatest increase observed in *ob/ob*-RC mice (**Table S4**). There was a high proportion of PUFAs in both diets, and consequently the HF-fed and WT-RC mice had similarly high PUFA content. The *ob/ob*-RC mice however had significantly lower PUFA compared to diet, presumably as a consequence of increased DNL and MUFA production. In summary, we have determined differences in both fatty acid content, and intact lipid species in liver tissue that are not attributable to diet alone, and are likely to arise from NAFLD or the metabolic context from which NAFLD arises.

NAFL is associated with changes to lipid zonation

Next we sought to address if lipids were differentially distributed in WT-RC control liver, and how such zonal patterns were affected with NAFL. Using MALDI-MSI, lipids were directly ablated from the surface of tissue, retaining spatial information that could be linked back to histology. Typically MALDI

spectra of liver tissue (**Figure S1A**) were composed primarily of potassiated PCs and their corresponding fragment ions (**Table S5-S6**). PCA was employed to comprehensively evaluate the spatial distribution of lipids in an unsupervised manner. PCA scores were visualised as a contour plot for each principal component. The first two principal components typically corresponded to histological features of interest with further components, representing successively less variation, attributed to artefacts of matrix deposition and tissue/matrix borders (**Figure 2A, 2C**). The loadings plot associated with each principal component represents the lipid species most important for discriminating regions (**Figure 2B, 2D**). For instance, SM(40:1) (*m/z* 825.622; $[M+K^+]$) and PC(32:0) (*m/z* 772.523; $[M+K^+]$) were predominantly located in the central vein or portal vein, respectively (**Figure 2E**). This was reflected in the scores and loadings plot for the first principal component. Zones 1 and 3 could be distinguished based on their lipid profiles and subsequent PCA scores in the second principal component (**Figure 2C-2D**). In particular, PC(36:3) (m/z 822.538; $[M+K^+]$) showed a strong zone 1 distribution, whilst PC(34:2) (m/z 796.522; $[M+K^+]$) was predominantly located in zone 3 (**Figure 2E**). Method reproducibility was assessed by comparing across serial sections from the same sample (**Figure S3**).

We went on to compare the WT-RC liver tissue (**Figure 3A**) with tissue from NAFL groups with different extents of steatosis and inflammation (**Figure 3B-3C**). Using the PCA scores and loadings plots and cross-referencing to adjacent H&E stained sections (**Figure 3**), we identified lipids with strong and reproducible zone 1 or zone 3 distributions (**Figure 3D-3E**). Whilst PC(32:0) and SM(40:1) were typically the major lipids observed in portal vein and central vein, respectively, for all groups, changes were observed in the lipids located in zones 1 and 3 (**Figure 3D-3E**). For instance, PC(34:2) was distributed mainly in zone 3 in WT-RC and WT-HF mice (**Figure 3A**) but in zone 1 in *ob/ob*-HF (**Figure 3C, 3E**). Of particular interest were AA-containing PC(38:4) (*m/z* 848.553; $[M+K^+]$; fatty acid composition 18:0/20:4), which became more strongly localised in zone 3 for *ob/ob* mice, and

docosahexaenoic acid (DHA)-containing PC(38:6) (*m/z* 844.522; [M+K$^+$]; 16:0/22:6) which shifted from zone 1 in WT mice to zone 3 in *ob/ob* mice (**Figure 3D; Figure S4**). This was mirrored to a certain extent by PC(40:7) (16:1/22:6) and PC(40:6) (16:0/22:6) (**Figure 3D**).

NASH leads to further increase in monounsaturated fat and loss of zonation

Having assessed the changes to lipid abundances and distributions in NAFL mice, we went on to similarly assess mouse models of NASH. Initially we sought to use the well-established methionine choline deficient (MCD) diet in mice to model NASH. We first assessed the hepatic lipid profile of MCD mice, compared to their methionine choline sufficient (MCS) controls by LC-MS (**Figure S5**). We were intrigued to note increased FFA(22:6) and long chain TAGs containing 22:6, whereas MUFAs were decreased or unchanged. Coupled with the knowledge that the MCD challenge induces weight loss, we interpret these results as a possible consequence of adipose tissue lipolysis (32, 33). We therefore opted for a Western diet (WD) to model NASH, since this can recapitulate the metabolic features of human NASH, whilst inducing obesity in mice (34-36).

NASH was induced in WT mice by WD-feeding for 32 weeks. The WD contained high levels of cholesterol, sucrose and saturated fat. A low fat (LFD) diet, with similar total fatty acid profile (**Table S4**), was used as a control diet. After 12 weeks, the mice on WD developed macro- and microvesicular steatosis, in contrast to the mice on LFD (**Figure 4A**). After 32 weeks, mice on WD developed NASH, with characteristic pericentral fibrosis (**Figure 4A**), increased serum ALT and transcripts for *Tnf-*α and *Tgf-*β*1* (**Figure 4B**).

The hepatic lipid profile was measured by LC-MS for mice on WD and LFD at 12 and 32 weeks, and the identified lipids used to construct a PCA model (**Figure 4C**). Interestingly, the four groups were clearly

distinguished (R^2 0.92, Q^2 0.88). The most important lipids which distinguished the WD-32 week mice from the others were TAG(54:3) (18:1/18:1/18:1) and TAG(52:2) (16:0/18:1/18:1), highlighting the importance of increased 18:1 as a marker for both NAFL and NASH (**Figure 4C**). We confirmed the increased 18:1 by GC-MS, measuring total hepatic fatty acid profiles for all samples and their diets (**Figure S2, Table S4**). The MUFA: SFA and SCD1 ratio were substantially increased by WD feeding, with the highest levels determined for the 32-week WD mice (2-fold increase).

Next we examined the zonal distribution of lipids in LFD and WD mice using MALDI-MSI (**Figure 4D-4F**). Consistent with our earlier findings, PC(32:0) and SM(40:1) were associated with portal and central vein respectively. AA-containing lipids PC(36:4) and PC(38:4) were located primarily in zone 3 for LFD and WD-12 week mice, whilst PC(34:1) and PC(32:1) were the major lipids in zone 1 (**Figure 4F**). It was extremely difficult to build a statistical model for zonal differences in WD-32 week mice however, with zonal distributions for most lipids being relatively weak or absent (**Figure 4E-4F**). This is exemplified by SM(40:1), normally associated with central vein (**Figure 4D**), however becoming increasingly delocalised with disease progression.

Lipid zonation in human NAFL and NASH

Human liver samples, covering the spectrum of NAFLD from normal to cirrhotic (**Figure 5A**), were analysed by LC-MS to compared the overall lipid profiles (**Figure S6**). We were specifically interested in the differences between liver presenting NAFL compared to NASH (**Figure 5B**). Multivariate analysis of these two groups revealed that samples with NASH had increased FFA(18:1) and short chain TAGs, including TAG(52:2) (16:0/18:1/18:1), compared to samples with steatosis only. This was confirmed by GC-MS (**Table S4**), and an increase in SCD1 activity implicated in human NAFL and NASH, in excellent agreement with the mouse studies.

Next we performed MALDI-MSI, using adjacent H&E stained sections and principal components analysis to identify histological regions and quantify the zonation of lipids (**Figure 5C**). Similar to the mouse samples, the portal vein was characterised by PC(32:0), whilst SM(40:1) was found to be associated with both central and portal veins. Interestingly, there was little difference observed between the zonal distributions of lipids in normal and NAFL liver tissue. In both groups PC(34:2) and PC(36:4) were the most predominant lipids in zone 1, whereas PC(34:1) and PC(36:1) were strongly associated with zone 3 (**Figure 5C-5D**). With NAFL progression to NASH, however the differences between pericentral and periportal regions became less pronounced, with partial to complete loss of zonation (**Figure 5C-5D**). Cirrhotic liver was characterised by nodular and fibrotic regions, rather than the traditional lobular structure (**Figure S7, Figure 5D**). Areas of fibrosis were characterised by increased PC(32:0) and SM species, whereas nodules had increased PC(34:1) and PC(32:1) (**Figure S7**).

Eicosanoid metabolism with NAFLD progression

Eicosanoids and lipid mediators are fatty acid metabolites and have been implicated in the inflammation response, and in the progression of NAFL to NASH. We therefore extracted these metabolites from homogenised mouse and human liver tissue and analysed the extracts by LC-MS/MS (**Figure S8**, **Table S3**). Overall, we detected 34 different eicosanoids and lipid mediators including AA-derived hydroxyeicosatetranoic acids (HETEs, 6), epoxyeicosatrienoic acids (EETs, 2), dihydroxyeicosatrienoic acids (DHETs, 3), prostaglandins (6); linoleic acid (LA)-derived hydroxyoctadecadienoic acids (HODEs, 2), epoxyoctadecaneoic acids (EpOMEs, 2), dihydroxyoctadecanoic acids (DiHOMEs, 2); eicosapentaenoic acid (EPA)-derived hydroxyeicosapentaenoic acids (HEPEs, 4) and DHA-derived hydroxydocosahexaenoic acids (HDoHEs, 2).

The resulting hepatic eicosanoid profiles were used to construct OPLS-DA models to discriminate between WT-RC control and NAFL mice (WT-HF, *ob/ob*-RC, *ob/ob*-HF) (**Figure S9**). The most discriminating class of eicosanoids for control and NAFL liver were the HEPEs, HDoHEs, and HETEs (**Figure S9D**). In particular, *n-3* DHA-derived 13-HDoHE and several *n-3* EPA-derived HEPEs were significantly decreased in *ob/ob* mice and by HF-feeding (**Figure 6A**). In contrast, *n-6* AA-derived 12- and 15-HETE were significantly increased by HF-feeding alone, whilst 5- and 11-HETE were significantly increased in *ob/ob* mice and by HF-diet (**Figure 6A**). Next we assessed the eicosanoid profiles from the WD/LFD mice, finding decreased 13-HDoHE in WD-fed mice, however no significant differences were noted in HETEs (**Figure 6B**).

We assessed similar metabolites in human liver, and determined that the concentrations of 9- and 13-HODE, regulated by LOX and derived from *n-6* fatty acid LA, were the most discriminating for NAFL and NASH, with both increased in NASH (**Figure 6C**), whilst there was no difference in 15-HETE concentration. Given that HETEs and HODEs are pro-inflammatory metabolites, we further examined how their levels were correlated with the pathologist-annotated "inflammation score", finding increased levels with higher scores ($p < 0.1$ for 13-HODE and 15-HETE).

Remodelling of phospholipid membrane feeds into upregulated eicosanoid synthesis

AA is incorporated into the membrane by the action of acyl transferases, notably LPCAT2, whilst group IVA phospholipase A2 (cPLA2) preferentially cleaves PC to release free AA, which is then metabolised by LOX to form HETEs and other eicosanoids (**Figure 7A**). An increase in AA-derived HETEs can be therefore be explained by higher amounts of AA-containing intact lipid in the membrane, increased availability of free AA, increased activity of the LOX pathway, or a combination of the above. To

elucidate which of these pathways are upregulated in NAFL, we measured hepatic mRNA levels for *Lpcat2, cPla2, Alox15* (15-LOX), *Alox5* (5-LOX) and *Alox12* (12-LOX) in WT-RC control and the three corresponding NAFL groups. A significant increase in hepatic mRNA levels for *Lpcat2* and *cPla2* was observed with NAFL in WT-HF, *ob/ob*-RC and *ob/ob*-HF mice, whereas *Alox15* was significantly increased by high fat feeding only (**Figure 7B**). No change was noted for *Alox12* or *Alox5* across the groups.

Hepatic transcript levels were measured for the mice fed WD or LFD for 12 and 32 weeks. Interestingly, there was a significant increase in *Lpcat2* (4-fold) and cPla2 (3-fold) for the mice which developed NASH (32 weeks WD), whilst no change in *Alox15* was observed across groups (**Figure 7C**). Similarly, hepatic mRNA levels for *LPCAT2, cPLA2* and *ALOX15* in human liver samples were measured (**Figure 7D**). *LPCAT2* and *cPLA2* were increased by up to 3-fold in NASH compared to NAFL, whilst *ALOX15* was significantly increased by up to 6-fold. It is worth noting that human 15-LOX prefers LA as a substrate producing 13-HODE, whereas the equivalent murine enzyme acts on AA to generate 15-HETE. Overall despite differences, the agreement between mouse and human data is striking, and may suggest a conserved mechanism of NAFLD progression.

Discussion

Here we established the zonal distributions of phospholipids in liver with NAFLD progression, using mouse models of NAFL and NASH, and clinical samples covering a range of NAFLD severity. Overall, both similarities and differences were found between the mouse and human studies. Similar lipids were found associated with portal and central veins, whilst many of the periportal/pericentral zonation patterns were opposite. For instance, PC(34:2) and PC(36:4) are typically zone 3 in mice and zone 1 in humans; PC(34:1) is typically zone 1 in mice and zone 3 in humans. However, in both mouse and human NASH, there was a striking loss in lipid zonation.

Previous studies have shown knockouts of either *Alox15* (37) or *cPla2* (38, 39) in mice resulted in reduced steatosis and inflammation emphasizing the importance of these pathways in NAFLD. Our data provide evidence at the metabolite and gene expression level for remodelling of the hepatic PC component in NAFLD. Specifically, we show that the activities of LPCAT2, cPLA2 and 15-LOX are upregulated in NAFL and NASH. This results in a cycle of AA enrichment and release from the membrane, generation of pro-inflammatory eicosanoids, followed by reintroduction of AA into membrane phospholipids (**Figure 7A**). Our data further show transcript levels for *LPCAT2* and *cPLA2* to be closely correlated in both the mice studies and the human study, suggesting that these two genes may be co-regulated (**Figure 7E**). Phospholipid remodelling in obesity has been linked to ER stress and disrupted calcium signalling (40). Given that the activities of both LPCAT2 and cPLA2 are calcium-dependent, further elucidation of the relationships between ER stress, calcium signalling and lipid remodelling in NAFLD may be warranted.

Of particular interest in this study is LPCAT2, which reintroduces PUFA - notably AA, into the membrane. Using immunohistochemistry, we found higher staining for LPCAT2 protein in zone 1 for WT mice and in zone 3, particularly around regions of steatosis, for *ob/ob* mice (**Figure 7F**). The specific zonation of LPCAT2 protein, in addition to its increased gene expression, may account for the enrichment of AA-containing PCs in zone 3, which was noted in the MSI experiments for murine NAFL. In contrast, LPCAT2 protein is pericentrally located in normal and NAFL human liver (**Figure 7F**). Since AA-containing PCs are typically periportal in human liver, an enrichment of LPCAT2 and AA in zone 3 would contribute to a loss of zonation for this lipid, which we observed in NASH. Whilst it is not clear whether the change in lipid zonation is a cause or effect of NAFLD, there does appear to be a link.

As a result of enrichment of AA in zone 3, generated eicosanoids will provide an inflammatory insult to hepatocytes in the pericentral region in particular. This may account for the increased oxidative damage observed in this region during NASH. Furthermore, since LPCAT2 is induced by pro-inflammatory cytokines (41, 42) and is highly expressed in inflammatory cells such as macrophages and neutrophils (41), this could further reinforce the inflammation cascade. We stained for CD68-positive cells (Kupffer cells, macrophages, monocytes; **Figure S10**) and found that these cells were distributed azonally in normal and NAFL human liver but in NASH were pericentrally located (also noted in (43)). Similarly, in human and murine NASH, LPCAT2 staining was highest surrounding pericentrally-located lipid droplets (**Figure S11-S12**) and inflammatory infiltrates. Taken together, this leads us to speculate that lipid droplet biology and macrophage infiltration may be important factors in the lipid remodelling observed during NAFLD.

Overall this study has described the location of lipids and their associated metabolic pathways in NAFL and NASH. We provide a link between the upregulation of enzymes involved in membrane remodelling, fatty acid release, eicosanoid formation, and lipid composition, whilst suggesting areas of interest for future study. The integration of mass spectrometry imaging technology with computational tools and traditional biochemical techniques has been shown here as a powerful approach. Importantly, this has enabled the fatty acid content of intact phospholipids to be mapped to particular locations in tissue and presents the opportunity to follow changes to lipid composition and distribution with disease state.

Acknowledgements

We thank Antonio Moschetta (University of Bari Aldo Moro) for sharing MCD mouse samples. The Disease Model Core of the MRC/WT Metabolic Research Laboratories of the University of Cambridge are thanked for technical support with animal experiments; Yajing Chu, Evelina Charidemou and

Steven Murfitt are thanked for laboratory assistance. The Human Research Tissue Bank is supported by the NIHR Cambridge Biomedical Research Centre. The Core Biochemical Assay Laboratory of Cambridge University Hospitals NHS Foundation Trust performed liver function tests.

References

1. Yeh MM, Brunt EM. Pathological features of fatty liver disease. Gastroenterology 2014;147:754-764.
2. Wree A, Broderick L, Canbay A, Hoffman HM, Feldstein AE. From NAFLD to NASH to cirrhosis-new insights into disease mechanisms. Nat Rev Gastroenterol Hepatol 2013;10:627-636.
3. Vacca M, Allison M, Griffin JL, Vidal-Puig A. Fatty Acid and Glucose Sensors in Hepatic Lipid Metabolism: Implications in NAFLD. Semin Liver Dis 2015;35:250-261.
4. Sanders FWB, Griffin JL. De novo lipogenesis in the liver in health and disease: more than just a shunting yard for glucose. Biol. Rev. 2016;91:452-468.
5. Tilg H, Moschen AR. Evolution of inflammation in nonalcoholic fatty liver disease: The multiple parallel hits hypothesis. Hepatology 2010;52:1836-1846.
6. Lambert JE, Ramos–Roman MA, Browning JD, Parks EJ. Increased De Novo Lipogenesis Is a Distinct Characteristic of Individuals With Nonalcoholic Fatty Liver Disease. Gastroenterology 2014;146:726-735.
7. Gorden DL, Myers DS, Ivanova PT, Fahy E, Maurya MR, Gupta S, Min J, et al. Biomarkers of NAFLD progression: a lipidomics approach to an epidemic. J Lipid Res 2015;56:722-736.
8. Loomba R, Quehenberger O, Armando A, Dennis EA. Polyunsaturated fatty acid metabolites as novel lipidomic biomarkers for noninvasive diagnosis of nonalcoholic steatohepatitis. J Lipid Res 2015;56:185-192.
9. Oresic M, Hyotylainen T, Kotronen A, Gopalacharyulu P, Nygren H, Arola J, Castillo S, et al. Prediction of non-alcoholic fatty-liver disease and liver fat content by serum molecular lipids. Diabetologia 2013;56:2266-2274.
10. Puri P, Baillie RA, Wiest MM, Mirshahi F, Choudhury J, Cheung O, Sargeant C, et al. A lipidomic analysis of nonalcoholic fatty liver disease. Hepatology 2007;46:1081-1090.
11. Puri P, Wiest MM, Cheung O, Mirshahi F, Sargeant C, Min HK, Contos MJ, et al. The plasma lipidomic signature of nonalcoholic steatohepatitis. Hepatology 2009;50:1827-1838.
12. Hijmans BS, Grefhorst A, Oosterveer MH, Groen AK. Zonation of glucose and fatty acid metabolism in the liver: mechanism and metabolic consequences. Biochimie 2014;96:121-129.
13. Berry KA, Hankin JA, Barkley RM, Spraggins JM, Caprioli RM, Murphy RC. MALDI imaging of lipid biochemistry in tissues by mass spectrometry. Chem Rev 2011;111:6491-6512.
14. Addie RD, Balluff B, Bovee JV, Morreau H, McDonnell LA. Current State and Future Challenges of Mass Spectrometry Imaging for Clinical Research. Anal Chem 2015;87:6426-6433.
15. Angel PM, Caprioli RM. Matrix-assisted laser desorption ionization imaging mass spectrometry: in situ molecular mapping. Biochemistry 2013;52:3818-3828.
16. Wattacheril J, Seeley EH, Angel P, Chen H, Bowen BP, Lanciault C, Caprioli RM, et al. Differential intrahepatic phospholipid zonation in simple steatosis and nonalcoholic steatohepatitis. PLoS One 2013;8:e57165.
17. Le Naour F, Bralet MP, Debois D, Sandt C, Guettier C, Dumas P, Brunelle A, et al. Chemical imaging on liver steatosis using synchrotron infrared and ToF-SIMS microspectroscopies. PLoS One 2009;4:e7408.

18. Debois D, Bralet MP, Le Naour F, Brunelle A, Laprevote O. In situ lipidomic analysis of nonalcoholic fatty liver by cluster TOF-SIMS imaging. Anal Chem 2009;81:2823-2831.
19. Bellafante E, Murzilli S, Salvatore L, Latorre D, Villani G, Moschetta A. Hepatic-specific activation of peroxisome proliferator-activated receptor γ coactivator-1β protects against steatohepatitis. Hepatology 2013;57:1343-1356.
20. Bedossa P, Poitou C, Veyrie N, Bouillot J-L, Basdevant A, Paradis V, Tordjman J, et al. Histopathological algorithm and scoring system for evaluation of liver lesions in morbidly obese patients. Hepatology 2012;56:1751-1759.
21. Sud M, Fahy E, Cotter D, Brown A, Dennis EA, Glass CK, Merrill AH, et al. LMSD: LIPID MAPS structure database. Nucleic Acids Research 2007;35:D527-D532.
22. Hsu F-F, Bohrer A, Turk J. Formation of Lithiated Adducts of Glycerophosphocholine Lipids Facilitates their Identification by Electrospray Ionization Tandem Mass Spectrometry. Journal of the American Society for Mass Spectrometry 1998;9:516-526.
23. Folch J, Lees M, Stanley GHS. A SIMPLE METHOD FOR THE ISOLATION AND PURIFICATION OF TOTAL LIPIDS FROM ANIMAL TISSUES. Journal of Biological Chemistry 1957;226:497-509.
24. Hall Z, Ament Z, Wilson CH, Burkhart DL, Ashmore T, Koulman A, Littlewood T, et al. Myc expression drives aberrant lipid metabolism in lung cancer. Cancer Research 2016;76:4608-4618.
25. Wiklund S, Johansson E, Sjöström L, Mellerowicz EJ, Edlund U, Shockcor JP, Gottfries J, et al. Visualization of GC/TOF-MS-Based Metabolomics Data for Identification of Biochemically Interesting Compounds Using OPLS Class Models. Analytical Chemistry 2008;80:115-122.
26. Trygg J, Wold S. Orthogonal projections to latent structures (o-PLS). J Chemometrics 2002;16:119-128.
27. van den Berg RA, Hoefsloot HC, Westerhuis JA, Smilde AK, van der Werf MJ. Centering, scaling, and transformations: improving the biological information content of metabolomics data. BMC Genomics 2006;7:142.
28. Rompp A, Schramm T, Hester A, Klinkert I, Both JP, Heeren RM, Stockli M, et al. imzML: Imaging Mass Spectrometry Markup Language: A common data format for mass spectrometry imaging. Methods Mol Biol 2011;696:205-224.
29. Takahashi Y, Soejima Y, Fukusato T. Animal models of nonalcoholic fatty liver disease/nonalcoholic steatohepatitis. World J Gastroenterol 2012;18:2300-2308.
30. Nilsson C, Raun K, Yan FF, Larsen MO, Tang-Christensen M. Laboratory animals as surrogate models of human obesity. Acta Pharmacol Sin 2012;33:173-181.
31. Wang X, West JA, Murray AJ, Griffin JL. Comprehensive Metabolic Profiling of Age-Related Mitochondrial Dysfunction in the High-Fat-Fed ob/ob Mouse Heart. J Proteome Res 2015;14:2849-2862.
32. Yew Tan C, Virtue S, Murfitt S, Roberts LD, Phua YH, Dale M, Griffin JL, et al. Adipose tissue fatty acid chain length and mono-unsaturation increases with obesity and insulin resistance. Scientific Reports 2015;5:18366.
33. Jha P, Knopf A, Koefeler H, Mueller M, Lackner C, Hoefler G, Claudel T, et al. Role of adipose tissue in methionine–choline-deficient model of non-alcoholic steatohepatitis (NASH)(). Biochimica et Biophysica Acta 2014;1842:959-970.
34. Machado MV, Michelotti GA, Xie G, de Almeida TP, Boursier J, Bohnic B, Guy CD, et al. Mouse Models of Diet-Induced Nonalcoholic Steatohepatitis Reproduce the Heterogeneity of the Human Disease. PLoS ONE 2015;10:e0127991.
35. Anstee QM. Animal models in nonalcoholic steatohepatitis research: utility and clinical translation. Liver international : official journal of the International Association for the Study of the Liver 2011;31:440-442.
36. Hebbard L, George J. Animal models of nonalcoholic fatty liver disease. Nat Rev Gastroenterol Hepatol 2011;8:35-44.

37. Martinez-Clemente M, Ferre N, Titos E, Horrillo R, Gonzalez-Periz A, Moran-Salvador E, Lopez-Vicario C, et al. Disruption of the 12/15-lipoxygenase gene (Alox15) protects hyperlipidemic mice from nonalcoholic fatty liver disease. Hepatology 2010;52:1980-1991.
38. Ishihara K, Miyazaki A, Nabe T, Fushimi H, Iriyama N, Kanai S, Sato T, et al. Group IVA phospholipase A2 participates in the progression of hepatic fibrosis. FASEB J 2012;26:4111-4121.
39. Ii H, Yokoyama N, Yoshida S, Tsutsumi K, Hatakeyama S, Sato T, Ishihara K, et al. Alleviation of high-fat diet-induced fatty liver damage in group IVA phospholipase A2-knockout mice. PLoS One 2009;4:e8089.
40. Fu S, Yang L, Li P, Hofmann O, Dicker L, Hide W, Lin X, et al. Aberrant lipid metabolism disrupts calcium homeostasis causing liver endoplasmic reticulum stress in obesity. Nature 2011;473:528-531.
41. Hishikawa D, Hashidate T, Shimizu T, Shindou H. Diversity and function of membrane glycerophospholipids generated by the remodeling pathway in mammalian cells. Journal of Lipid Research 2014;55:799-807.
42. Tanaka N, Matsubara T, Krausz KW, Patterson AD, Gonzalez FJ. Disruption of phospholipid and bile acid homeostasis in mice with nonalcoholic steatohepatitis. Hepatology 2012;56:118-129.
43. Lefkowitch JH, Haythe JH, Regent N. Kupffer Cell Aggregation and Perivenular Distribution in Steatohepatitis. Mod Pathol 2002;15:699-704.

Figure Legends

Figure 1. Hepatic lipid signatures in murine NAFL. Increasing steatosis (WT-RC << WT-HF < *ob/ob*-RC $\approx$ *ob/ob*-HF) was assessed by Masson's trichrome staining (top; magnification x 200) and quantified (%) using oil red O lipid stain (bottom) (**A**). Serum alanine transaminase (ALT) was elevated in *ob/ob*-RC and *ob/ob*-HF groups, and a stepwise increase in hepatic mRNA levels for *Tnf-*α and *Tgf-*β*1* was observed in WT-HF, *ob/ob*-RC and *ob/ob*-HF groups; * $p < 0.05$, ** $p < 0.01$, *** $p < 0.001$ (**B**). Representative LC-MS chromatograms are shown for control (WT-RC) (**C**) and NAFL (*ob/ob*-HF) mouse liver (**D**). Lipids identified by LC-MS were used to construct principal components models (**E**), which clearly distinguish the four groups based on their lipid signatures. The associated loadings plot (**F**) shows the most important lipids for differentiating groups.

Figure 2. Principal components analysis (PCA) of imaging data reveal liver histology. PCA analysis was employed to evaluate the spatial distribution of lipids, illustrated here for control (WT-RC) mouse liver tissue. The PCA scores for the first two principal components were plotted against *x* and *y* coordinates (yellow and blue colours indicate most positive and negative scores, respectively). This

gave rise to contour plots which here correspond to regional differences in central vein/portal vein (CV/PV) (**A**) and Zone 1/Zone 3 (**C**). The corresponding loadings plots (**B** and **D**) represent which lipids (*m/z*) are most important for differentiating regions. Two-dimensional single ion distributions for SM(40:1) [M+K^+], PC(32:0) [M+K^+], PC(36:3) [M+K^+] and PC(34:2) [M+K^+] show a central vein, portal vein, zone 1 or zone 3 distribution respectively (**E**). Highest intensities are shown in yellow.

Figure 3. Lipid zonation in murine NAFL. Sections of mouse liver tissue were probed by MALDI-MSI or stained with H&E. Two-dimensional distributions for key ions (left) and PCA scores plots (right) closely recapitulate liver histology (middle). Key ion distributions show PC(36:3) [M+K^+] (red), PC(34:2) [M+K^+] (green), SM(40:1) [M+K^+] (blue) for **WT-RC** control mice (**A**); PC(36:2) [M+K^+] (red), PC(34:2) [M+K^+] (green), PC(32:0) [M+K^+] (blue) for **WT-HF** mice (**B**); PC(38:6) [M+K^+] (red), PC(38:4) [M+K^+] (green), PC(32:0) [M+K^+] (blue) for ***ob/ob*-HF** mice (**C**). Positive and negative PCA scores are associated with zones 1 and 3, respectively (yellow and blue colours indicate most positive and negative scores, respectively). PCA loadings plots (far right) show the lipids of greatest importance for differentiating zones. Histological features of interest are labelled (PV = portal vein, CV = central vein, Z1 = zone 1, Z3 = zone 3); *m/z* peaks labelled with asterisks are fragment ions. Zonation for different lipid species was quantified across biological replicates using PC loadings scores (**D-E**).

Figure 4. Lipid changes in a mouse model of NASH. Masson's trichrome staining (magnification x 100) reveals liver tissue from wild type (WT) mice on a Western diet (WD) for 12 weeks develop steatosis, and after 32 weeks develop NASH with fibrosis (stained blue; **A**)**.** Serum ALT and hepatic transcripts *Tnf-*α and *Tgf-*β*1* are elevated in 32 week WD mice compared to their low fat controls, and compared to 12 weeks WD (** $p < 0.01$, *** $p < 0.001$) (**B**). PCA and corresponding loadings plot for distinguishing the groups based on their hepatic intact lipid profiles determined by LC-MS (**C**). Spatial distribution of SM(40:1) across liver tissue shows increasing delocalisation with disease progression. Highest intensity is shown in yellow (**D**). Lipid zonation becomes less marked in 32-week WD mice, as determined by PC

scores; yellow and blue represent most positive and negative scores, respectively (**E**). Quantification of the corresponding PC loadings show that lipid zonation is almost completely lost with NASH (**F**).

Figure 5. Lipid distributions across the human NAFLD spectrum. H&E stained sections (magnification x 40) of human liver tissue ranging from normal, NAFL, NASH to cirrhosis (**A**). Homogenised liver tissue was analysed by LC-MS, and the lipidomic profile used to compare NAFL and NASH groups, revealing increased shorter chain TAGs, and FFA(18:1) in NASH (**B**). MALDI-imaging was performed on frozen sections of tissue, and quantified (**C**) revealing changes to zonation with NASH. Example MS images of tissue covering the spectrum of NAFLD are shown alongside corresponding adjacent H&E sections (**D**). Spatial distributions for PC(32:0) (portal vein), PC(36:4) and PC(34:1) are denoted as blue, red and green respectively for normal, NAFL and NASH. Greater intensity of colour reflects relative abundance. Whilst PC(36:4) and PC(34:1) are located in zones 1 and 3, respectively, in both normal and NAFL, there is partial to complete loss of zonation in NASH. Cirrhotic tissue on the other hand is marked by lipid changes to fibrotic and nodular regions (see supporting information). Spatial distributions for lipids denoted in blue, red and green for cirrhosis are PC(32:0), PC(34:1), PC(34:2), respectively.

Figure 6. Changes to eicosanoid lipid mediators with NAFLD. Decreased *n-3* fatty acid (eicosapentaenoic acid (EPA), DHA)-derived anti-inflammatory eicosanoids and increased *n-6* fatty acid (AA)-derived pro-inflammatory eicosanoids observed in liver from *ob/ob* mice and mice on a high fat diet. Two way ANOVA was performed to assess the contribution of the diet, genotype (KO) and their interaction (~) to the metabolite changes observed (**A**). Similarly, a decrease in *n-3* derived 13-HDoHE was noted for mice following a Western diet, whilst no significant difference was determined for the *n-6* derived HETEs (**B**). Significantly increased *n-6* LA-derived pro-inflammatory HODEs were observed in liver with NASH, compared to NAFL, in human liver tissue. Increased HETEs and HODEs ($p < 0.1$) were found in human samples with a higher inflammation score (**C**). Data are expressed as median ± upper/lower quartile (* $p < 0.05$, ** $p < 0.01$, *** $p < 0.001$).

Figure 7. Fatty acid remodelling in NAFLD. Group IVA phospholipase (cPLA2) preferentially cleaves phosphatidylcholine (PC) to release arachidonic acid (AA). AA can then be metabolised by lipoxygenases (LOX) to form eicosanoids, including pro-inflammatory HETEs. PCs are regenerated by the action of lysophosphatidycholine acyl transferases (LPCAT) on lysophosphatidylcholines (LysoPC) (**A**). An increase was observed in hepatic mRNA levels for *cPla2* and *Lpcat2* with high fat (HF) diet and for *ob/ob* mice (two way ANOVA). *Alox15* was significantly increased by HF-feeding only (**B**). Gene transcripts for *cPla2* and *Lpcat2* were significantly increased in mice fed a Western diet (WD) for 32 weeks (**C**). Similarly, hepatic mRNA levels for *cPLA2*, *LPCAT2* and *ALOX15* were all increased in human NASH compared to NAFL; * $p < 0.05$, ** $p < 0.01$, *** $p < 0.001$ (**D**). A striking correlation between *Lpcat2* and *cPLa2* mRNA levels were noted in both mouse and human studies (**E**). Immunostaining (magnification x 50) showed that LPCAT2 protein has a distinct periportal distribution in WT mice, and a pericentral distribution in *ob/ob* mice and human liver (**F**).

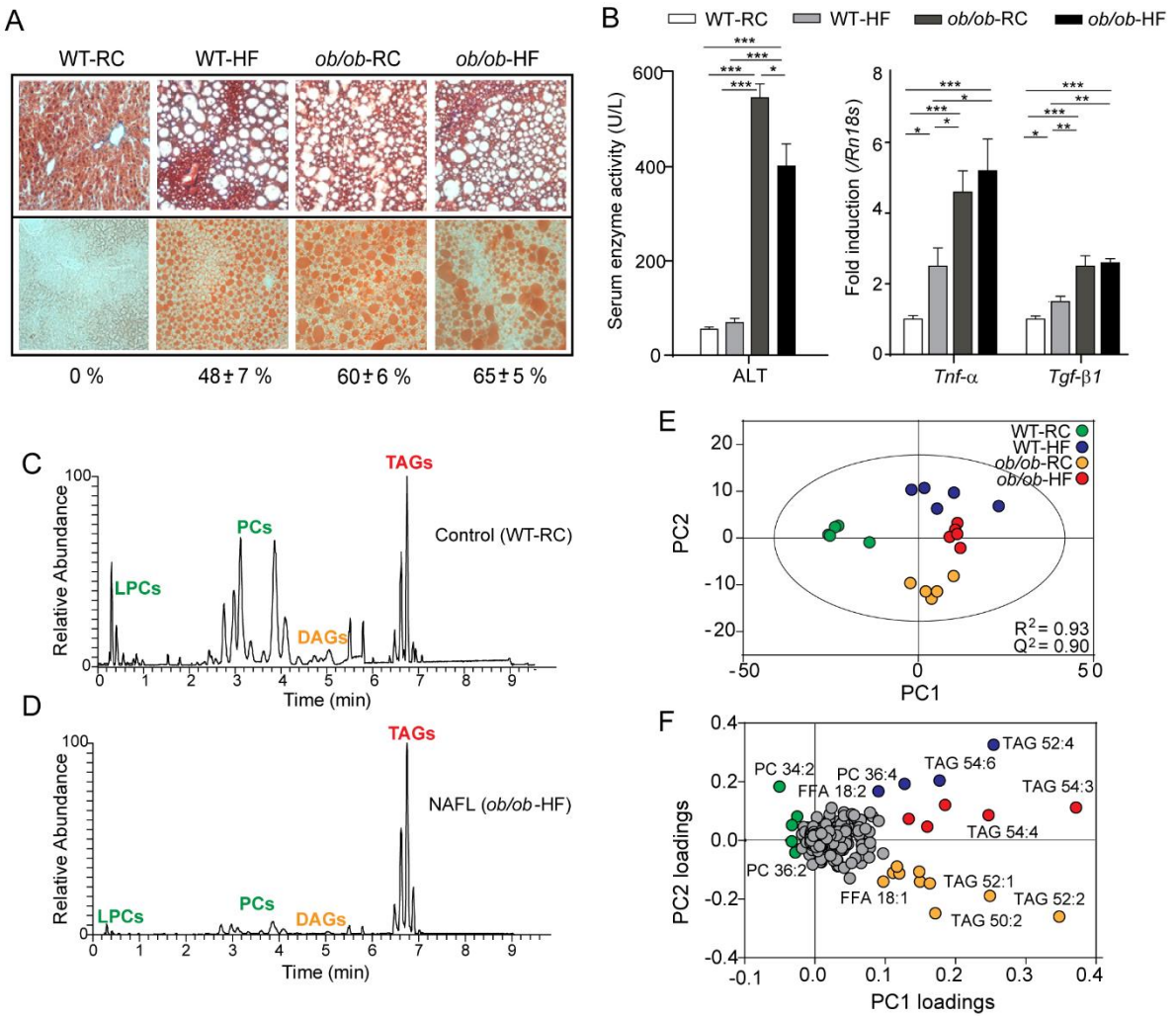
A
WT-RC
WT-HF
ob/ob-RC
ob/ob-HF
0 %
48 ± 7 %
60 ± 6 %
65 ± 5 %
B
WT-RC
WT-HF
ob/ob-RC
ob/ob-HF
Serum enzyme activity (U/L)
ALT
Fold induction (/Rn18s)
Tnf-α
Tgf-β1
C
Relative Abundance
Time (min)
LPCs
PCs
DAGs
TAGs
Control (WT-RC)
D
NAFL (ob/ob-HF)
E
PC2
PC1
R2 = 0.93
Q2 = 0.90
F
PC2 loadings
PC1 loadings
TAG 52:4
TAG 54:6
TAG 54:3
PC 34:2
PC 36:4
FFA 18:2
TAG 54:4
PC 36:2
TAG 52:1
FFA 18:1
TAG 52:2
TAG 50:2

Figure 1

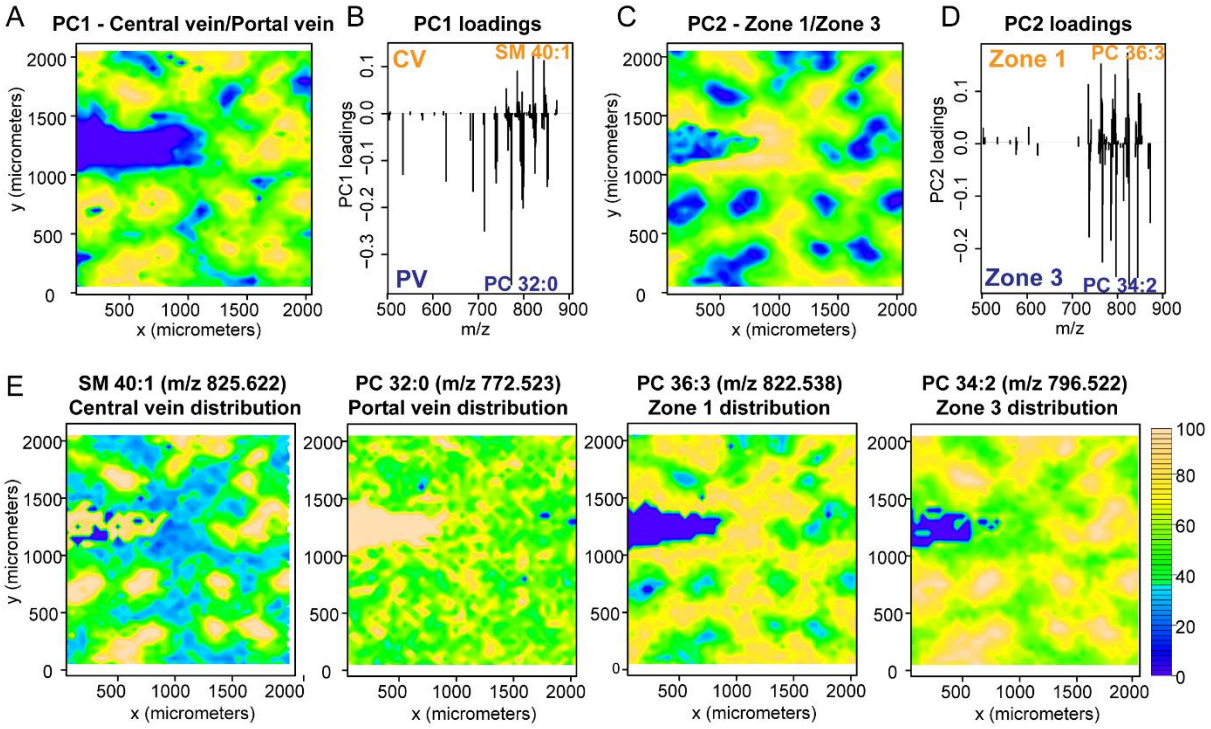
A
PC1 - Central vein/Portal vein
y (micrometers)
x (micrometers)
B
PC1 loadings
CV
SM 40:1
PV
PC 32:0
PC1 loadings
m/z
C
PC2 - Zone 1/Zone 3
y (micrometers)
x (micrometers)
D
PC2 loadings
Zone 1
PC 36:3
Zone 3
PC 34:2
PC2 loadings
m/z
E
SM 40:1 (m/z 825.622)
Central vein distribution
PC 32:0 (m/z 772.523)
Portal vein distribution
PC 36:3 (m/z 822.538)
Zone 1 distribution
PC 34:2 (m/z 796.522)
Zone 3 distribution
y (micrometers)
x (micrometers)

Figure 2

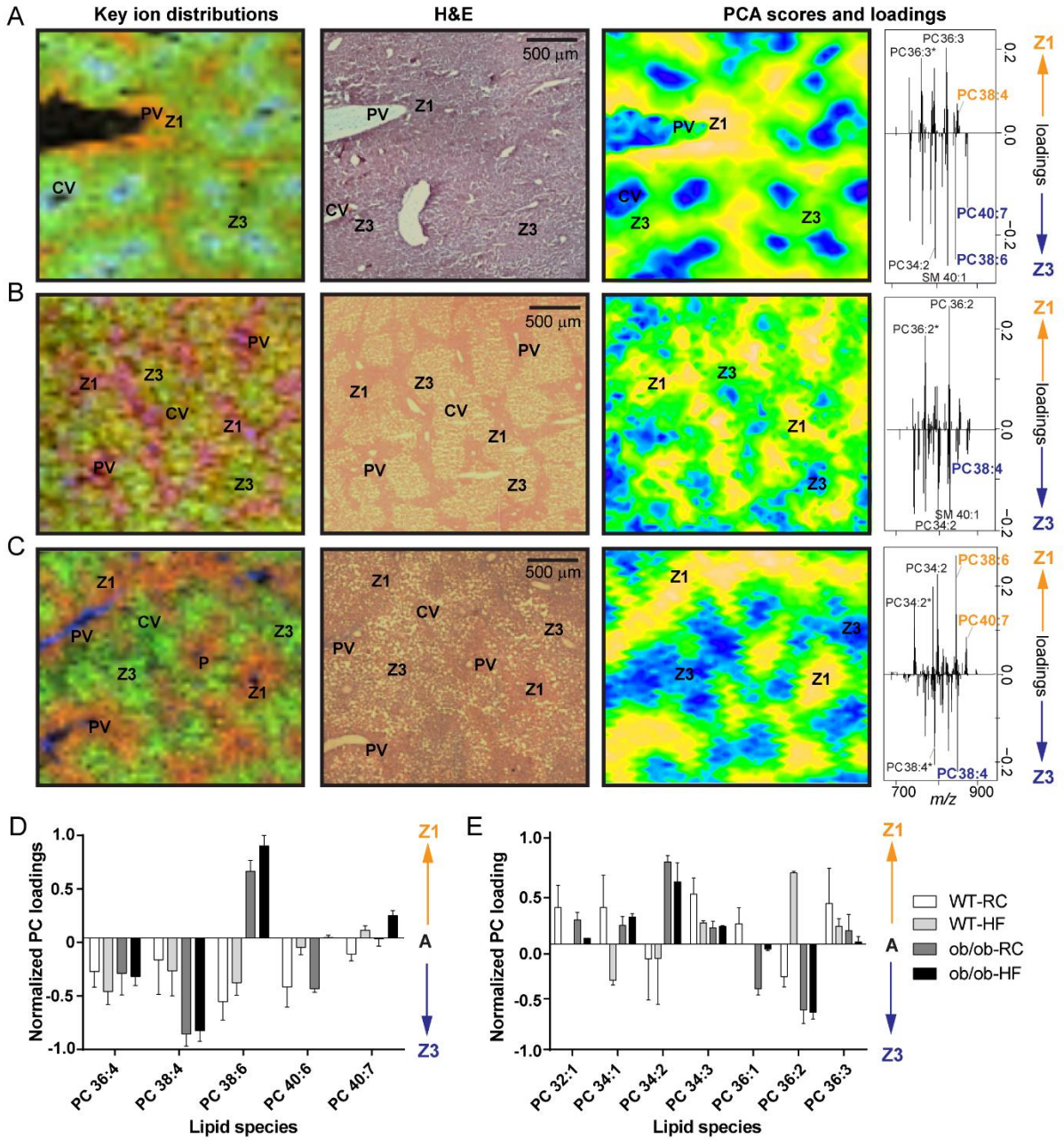
A
Key ion distributions
H&E
PCA scores and loadings
500 µm
PV
Z1
CV
Z3
PC36:3
PC36:3*
PC38:4
PC40:7
PC34:2
PC38:6
SM 40:1
loadings
B
PC 36:2
PC36:2*
C
PC34:2*
PC38:4*
700
900
m/z
D
Normalized PC loadings
A
PC 36:4
PC 38:4
PC 38:6
PC 40:6
PC 40:7
Lipid species
E
Normalized PC loading
PC 32:1
PC 34:1
PC 34:2
PC 34:3
PC 36:1
PC 36:2
PC 36:3
WT-RC
WT-HF
ob/ob-RC
ob/ob-HF

Figure 3

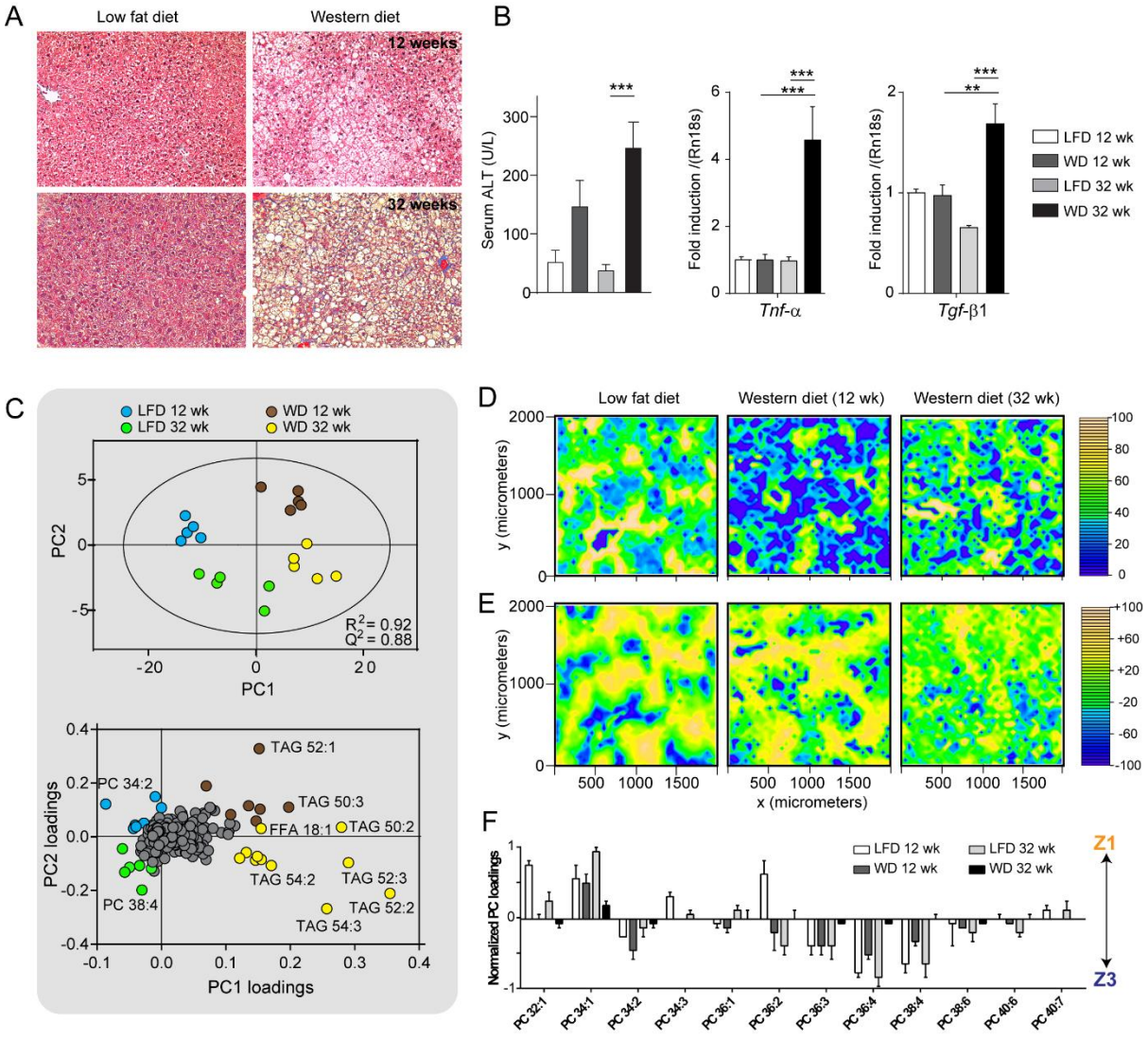
A
Low fat diet
Western diet
12 weeks
32 weeks
B
Serum ALT (U/L)
Fold induction /(Rn18s)
Tnf-α
Tgf-β1
LFD 12 wk
WD 12 wk
LFD 32 wk
WD 32 wk
C
PC2
PC1
R2= 0.92
Q2= 0.88
PC2 loadings
PC1 loadings
TAG 52:1
PC 34:2
TAG 50:3
FFA 18:1
TAG 50:2
TAG 54:2
TAG 52:3
PC 38:4
TAG 52:2
TAG 54:3
D
Low fat diet
Western diet (12 wk)
Western diet (32 wk)
y (micrometers)
E
x (micrometers)
F
Normalized PC loadings
Z1
Z3
PC 32:1
PC 34:1
PC 34:2
PC 34:3
PC 36:1
PC 36:2
PC 36:3
PC 36:4
PC 38:4
PC 38:6
PC 40:6
PC 40:7

Figure 4

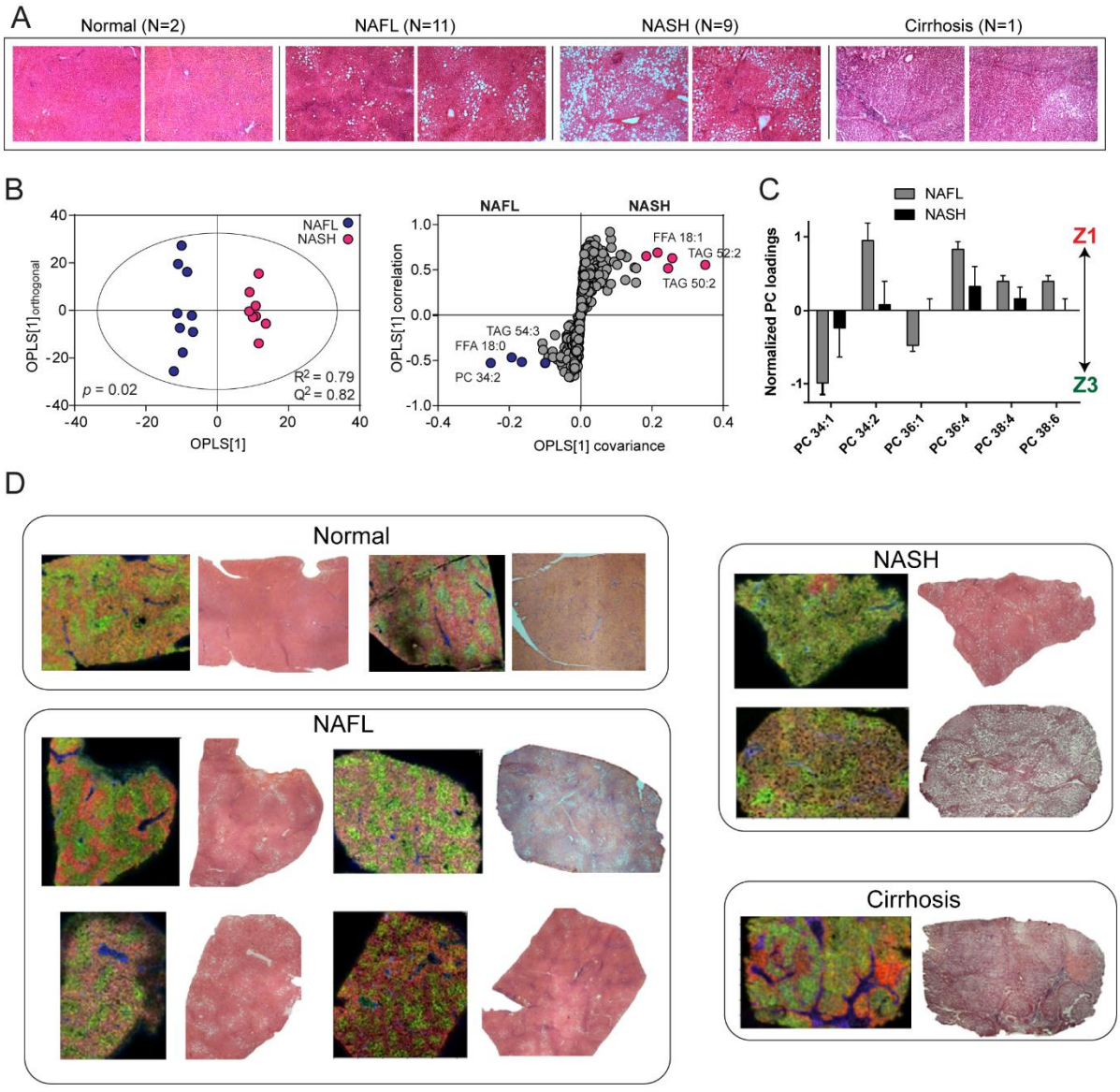
A
Normal (N=2)
NAFL (N=11)
NASH (N=9)
Cirrhosis (N=1)
B
NAFL
NASH
OPLS[1]orthogonal
OPLS[1]
p = 0.02
R2 = 0.79
Q2 = 0.82
NAFL
NASH
OPLS[1] correlation
OPLS[1] covariance
FFA 18:1
TAG 52:2
TAG 50:2
TAG 54:3
FFA 18:0
PC 34:2
C
NAFL
NASH
Normalized PC loadings
Z1
Z3
PC 34:1
PC 34:2
PC 36:1
PC 36:4
PC 38:4
PC 38:6
D
Normal
NAFL
NASH
Cirrhosis

Figure 5

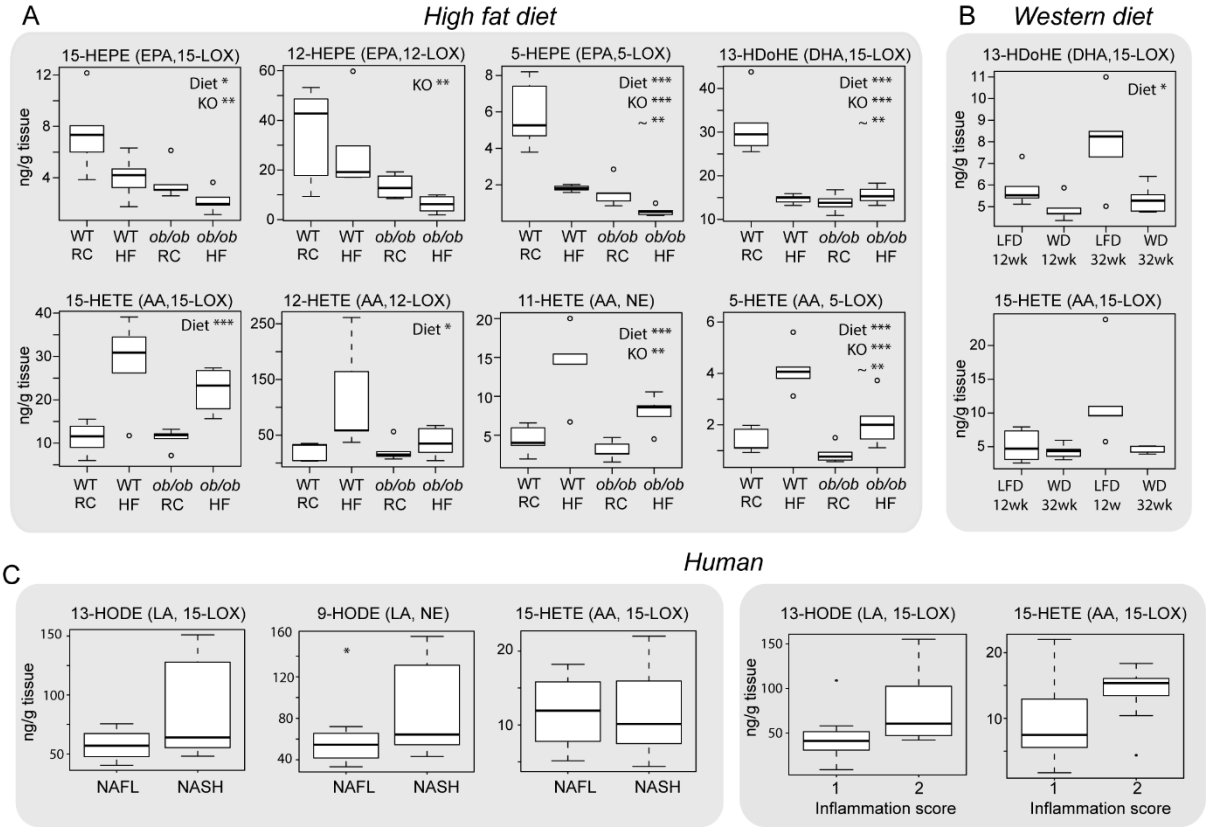
A
High fat diet
B
Western diet
15-HEPE (EPA,15-LOX)
12-HEPE (EPA,12-LOX)
5-HEPE (EPA,5-LOX)
13-HDoHE (DHA,15-LOX)
15-HETE (AA,15-LOX)
12-HETE (AA,12-LOX)
11-HETE (AA, NE)
5-HETE (AA, 5-LOX)
ng/g tissue
WT RC
WT HF
ob/ob RC
ob/ob HF
LFD 12wk
WD 12wk
LFD 32wk
WD 32wk
LFD 12w
WD 32wk
C
Human
13-HODE (LA, 15-LOX)
9-HODE (LA, NE)
15-HETE (AA, 15-LOX)
NAFL
NASH
Inflammation score

Figure 6

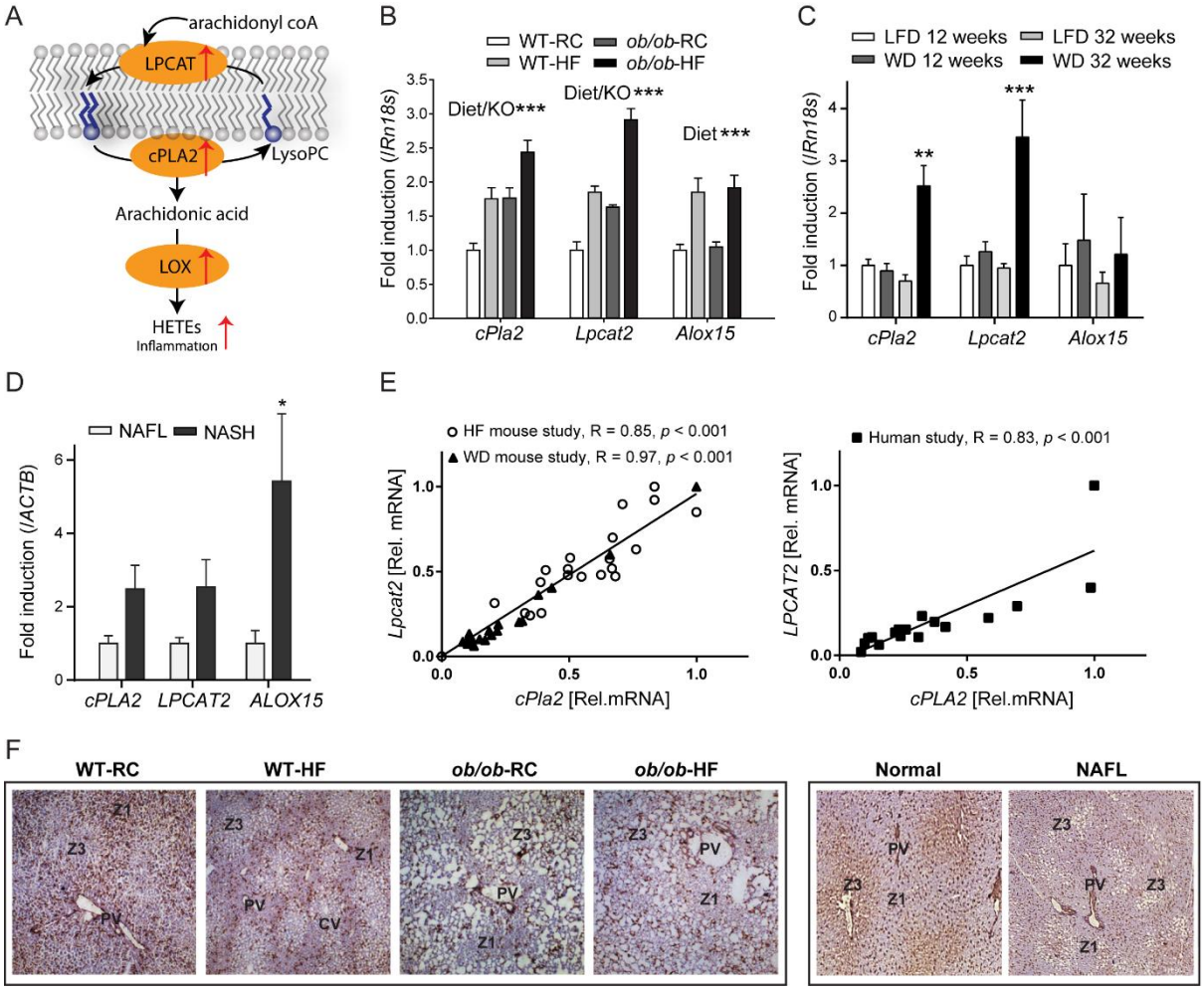
A
arachidonyl coA
LPCAT
cPLA2
LysoPC
Arachidonic acid
LOX
HETEs
Inflammation
B
WT-RC
WT-HF
ob/ob-RC
ob/ob-HF
Diet/KO***
Diet/KO***
Diet***
Fold induction (/Rn18s)
cPla2
Lpcat2
Alox15
C
LFD 12 weeks
LFD 32 weeks
WD 12 weeks
WD 32 weeks
**
***
Fold induction (/Rn18s)
cPla2
Lpcat2
Alox15
D
NAFL
NASH
*
Fold induction (/ACTB)
cPLA2
LPCAT2
ALOX15
E
HF mouse study, R = 0.85, p < 0.001
WD mouse study, R = 0.97, p < 0.001
Lpcat2 [Rel. mRNA]
cPla2 [Rel.mRNA]
Human study, R = 0.83, p < 0.001
LPCAT2 [Rel. mRNA]
cPLA2 [Rel.mRNA]
F
WT-RC
WT-HF
ob/ob-RC
ob/ob-HF
Normal
NAFL
Z1
Z3
PV
CV

Figure 7